ERS-1 Investigations of Southern Ocean Sea Ice Geophysics Using Combined Scatterometer and SAR Images.

Mark R. Drinkwater
Jet Propulsion Laboratory, California Institute of Technology,
4800 Oak Grove Dr. Pasadena, California 91109 USA
Tel: (813) 354-8189 Fax: (818) 393-6720

David S. Early and David G. Long
Electrical and Computer Engineering Department,
Brigham Young University, 459 CB, Provo UT 84602 USA
Tel: (801) 378-4383 Fax: (801) 378-6586

Abstract Coregistered ERS-1 SAR and Scatterometer data are presented for the Weddell Sea, Antarctica. Calibrated image backscatter statistics are extracted from data acquired in regions where surface measurements were made during two extensive international Weddell Sea experiments in 1992. Changes in summer ice-surface conditions, due to temperature and wind, are shown to have a large impact on observed microwave backscatter values. Winter calibrated backscatter distributions are also investigated as a way of describing ice thickness conditions in different locations during winter. Coregistered SAR and EScat data over a manned drifting ice station are used to illustrate the seasonal signature changes occurring during the fall freeze-up transition. Combinations of Weddell Sea SAR and Scatterometer data are shown to be an extremely powerful tool for monitoring both sea-ice dynamics and the thermodynamic changes which accompany seasonal transitions in the Southern Ocean.

I. INTRODUCTION

Logistical constraints on the operating times of ERS-1 synthetic aperture radar (SAR) receiving stations in Antarctica results in restricted spatial and temporal SAR coverage. The fact that the German Antarctic Receiving Stations (GARS) at Bernardo O'Higgins is only manned for a limited number of six-week (continuous-operation) campaigns each year precludes more comprehensive studies of the seasonal influence on Southern Ocean sea-ice geophysical processes.

A method for supplementing mesoscale (100x100km) SAR scenes of ice conditions is proposed using non-imaging Scatterometer (EScat) mode data from the ERS-1 AMI instrument. This technique produces enhanced resolution C-band images from 500km swath, gridded EScat data, improving the nominal 50km resolution to 14km (Long et al., *this issue*). EScat images map the mean backscatter coefficient (*A*) normalized to 40° incidence, and the gradient in backscatter (*B*) across the 20-60° incidence angle range. Weekly EScat images of the entire Southern Ocean south of 55°, generated at intervals throughout the 1992 austral winter, enable sea-ice processes around Antarctica to be monitored. Such data complement 25m resolution 100km SAR images (at 20-26° incidence) acquired only during periods of operation of the GARS and the Japanese Antarctic receiving station (at Syowa). While AMI SAR image pairs provide detailed indications of the ice motion and sea-ice conditions on the 100km scale (Drinkwater and Kottmeier, *this issue*), time-integrated, medium-scale resolution, hemispheric coverage EScat images complement SAR by uninterrupted mapping of basin-scale dynamics and the processes of seasonal advance and decay of the entire Southern Ocean ice cover.

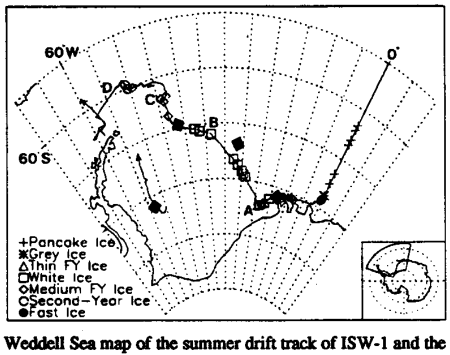

Figure 1. Weddell Sea map of the summer drift track of ISW-1 and the WWGS '92 track of R/V *Polarstern*. Sea ice characteristics are identified by symbols along the ship track, and SAR image locations are indicated by solid boxes.

II. FIELD EXPERIMENT OBSERVATIONS

In 1992, two large experiments were conducted in the Weddell Sea, Antarctica, and Fig. 1 shows a detailed map of the region of interest. The first experiment was the manned, drifting ice camp Ice Station Weddell (ISW-1). This camp was deployed on 6 February in summer, and drifted predominantly northwards during its lifetime (see Fig. 1), transiting the fall freeze-up period into the winter until a 7 June recovery. Its drift spanned the 3-day PIPOR orbit phase, lasting two months into the 35-day multidisciplinary orbit phase of ERS-1. SAR image acquisition opportunities during this period were thus limited to times when the ice station floe passed beneath an imaging swath (see solid square at 72°S 53°W). Overlapping EScat and SAR coverage of ISW-1 was achieved during the months of February and March at this location, and during this period continuous measurements were made of ice surface geophysics and meteorological and oceanographic conditions. Examples are shown later of the transition from summer into fall freeze-up, illustrated by backscatter signatures under various meteorological conditions. Time-series of these data are also used to illustrate the modification to backscattering signature characteristics as the ice around ISW underwent seasonal changes.

A second austral winter experiment called the Winter Weddell Gyre Study '92 was conducted by the German icebreaker R/V *Polarstern*. The transect in Fig. 1 shows the track of the vessel beginning in the east with a southward bound leg at the end of May 1992 following the 0° meridian to the Antarctic coast. This track turns west-south westwards along the ice shelf, reaching 73°S at point A by the end of June, 1992. At this southernmost location a northwestward course was selected to cross the Weddell Sea towards the South Orkneys. This path is interrupted only by a small course change at waypoint B and a 3-day drift station performed at location C. After passing around the islands, the ice edge was exited on 29 July, 1992 in the vicinity of location D in Fig. 1.

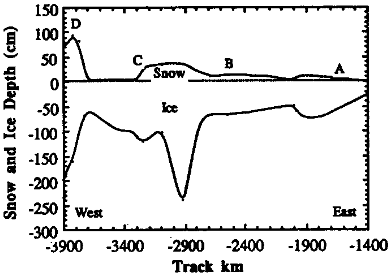

Figure 2. Interpolated fit to mean snow and sea-ice depths measured along the WWGS '92 transect. Waypoint markers A-B relate thicknesses to locations and ice types identified in Figure 1.

Symbols plotted along the length of the WWGS '92 *Polarstern* track indicate snow and sea-ice characteristics measurement sites. A legend in Fig. 1 indicates the ice types found in the Weddell Sea, and Fig. 2 shows snow and ice thicknesses corresponding with the 2500 km transect between points A and D. Figure 2 illustrates that Eastern Weddell Sea ice comprises largely undeformed local thermodynamic growth forms less than 70 cm thick. White ice of around 50 cm thick was the most predominant variety of first-year (FY) ice, especially between waypoints A and B. Such locally formed ice also had a shallow snow cover typically less than 20 cm deep. Moving northwestwards beyond waypoint B, a band of mixed ice forms was crossed. This comprised undeformed second-year, smooth first-year and well-deformed, rough first-year (FYR) ice floes. The latter had mean ice thicknesses exceeding 2.0 m in places. Between location C

0-7803-1497-2/94 $4.00 © 1994 IEEE

and D a swath of thinner FY ice is observed with little or no snow cover, before another band of thicker undeformed, low-salinity second-year (SY) ice was encountered. Drinkwater *et al.* (1993) proposed that this location is one of the principal regions of winter outflow of old ice from the Weddell and Bellingshausen Seas, due the extremely deep, layered snow cover recorded on such flat, high freeboard floes.

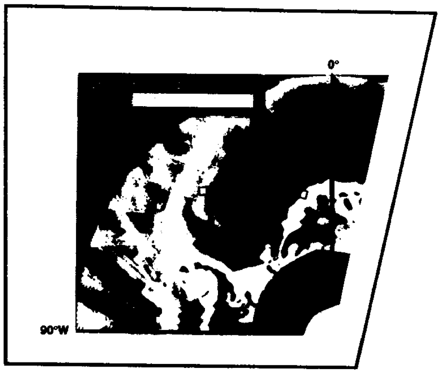

Figure 3. Enhanced resolution ERS-1 Scatterometer image of the Weddell Sea sector of the Southern Ocean during winter. Locations of SAR image data are shown by open boxes.

An EScat calibrated radar backscatter image shown in Figure 3 provides a regional context for the WWGS '92 observations of winter ice in the Weddell Sea. This image clearly indicates that C-band backscatter at 40° incidence is sensitive to some of the physical differences identified in this section. Relatively high backscatter is observed in the regions of old or deformed ice, while the predominantly divergent areas of relatively thin, undeformed ice tend to have lower backscatter values. A number of sites are chosen from which winter SAR image statistics are used in the following discussion of microwave signature variations.

III. SEASONAL SAR SIGNATURES OF WEDDELL SEA ICE

In this section, examples of overlapping calibrated C-band ERS-1 AMI signatures are used to illustrate various Weddell Sea summer ice signatures and contrasting winter ice conditions. Importantly, when the SAR is operating and acquiring high resolution image data, the Scatterometer mode switched off, and vice-versa. This means that EScat image data presented here are not simultaneous to the spatially overlapping SAR image data (as in Fig. 3). Instead, a weekly EScat image is chosen for comparison since it allows the SAR imaging time to be bracketed. A 7-day integration time enables a higher resolution (~14 km) scatterometer product and an incidence angle diverse backscatter coefficient, $\sigma^{\circ}(\theta)$ to be derived (Drinkwater *et al.*, 1993).

Summer Ice Signatures

Four SAR images were selected which characterise the sea ice around ISW-1 as it drifted through a fixed SAR swath cross-over in February and March 1992, during the 3-day repeat orbit (see location of solid square in Fig. 1). Full-resolution 16-bit 25m SAR images were sub-sampled to 100m resolution, then calibrated and geolocated, to enable comparisons with other forms of data. SAR data shown here illustrate backscatter values in the full 20-26° incidence-angle range.

SAR backscatter histograms are shown in Fig. 4a for; (1) day 32 (1 Feb.) - prior to ice camp deployment; (2) day 41 (10 Feb.); day 64 (4 Mar.); and day 74 (14 Mar.). These distributions are representative of mixtures of snow-covered second-year ice, which survived summer, and open water (see Drinkwater and Kottmeier, *this issue*, for SAR image example from ISW-1 on day 46). These four dates (in Fig. 4a) were selected by using the meteorological record from ISW-1 to subdivide the SAR imaging window into periods which were windy and warm (histogram 1), calm and warm (histogram 2) windy and cold (histogram 3), and calm and cold (histogram 4). Windy periods are characterized by wind speeds at ISW-1 of 8 m/s or more, while warm temperatures are classed as equal to or exceeding -10°C. In histogram 1, conditions were windy and mean air temperatures of -2.2°C ensured that the snow cover was still isothermal and at 0°C at depth. ISW-1 surface observations confirm that the snowcover was still relatively slushy after the summer melt, and thus the scattering mechanism causing a mean of -8.08 dB and peak value of -7 dB is predominantly rough surface scattering. Values below -10 dB indicate non wind-roughened leads, while the small tail at values exceeding -5 dB is caused by bright leads in this image. Histogram 2, 3-days later, shows a large change in the backscatter distribution for the case where the wind drops and the temperatures remain relatively warm. Previously, strong winds on day 38 helped cool the surface of the snow, by evaporation and turbulent fluxes of sensible and latent heat. Now the surface of the SY ice floes becomes a more effective scatterer and the peak shifts to -6 dB. Nonetheless, the most dramatic change is the increase in the contrast between the ice floes and leads, and a noticeable toe develops at lower backscatter values. As fall freeze-up begins, air temperatures fall below -10°C for the first time (on 28 February). Histogram 3 (on 4 March) shows a case of high winds and a mean air temperature of -11.9°C. As the snow layer on the ice floes begins to freeze the peak in the backscatter begins to fall, and for the first time lead-ice growth begins, pushing low-end values in the distribution below -15 dB. Since some open water still exists in leads, the upper end of the distribution remains tied at -7 dB. Subsequently, as fall freeze-up takes hold, temperatures drop below -20°C and histogram 4 on day 74 (14 March) illustrates a continuation of the progression to a lower mean value of -9.8 dB, a peak at -8.5 dB, and a reduction in high-end values.

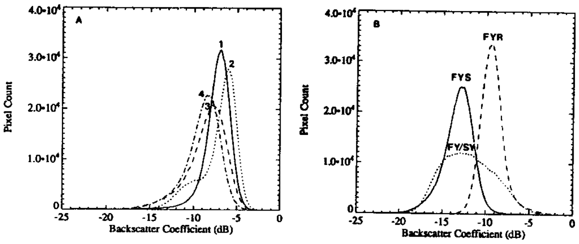

Figure 4. Calibrated ERS-1 SAR image histograms for (a) summer second-year ice around ISW-1 under varying wind and temperature conditions; and (b) winter first-year smooth (FYS), first-year rough (FYR) and mixed first- and second-year ice (FY/SY).

Figure 4a indicates that the signatures of this old ice pack are extremely dynamic and that the backscattering at 20-26° incidence is important from open water between ice floes when temperatures are warm. But, when ice growth begins in the leads (after day 64) the characteristics of the surface of the second-year ice floes become the dominant signature component. Examples of EScat data are compared with these SAR statistics later, to further illustrate the progression of fall freeze-up and point out the seasonal indicators which may be identified in time-series data.

Winter Ice Signatures

Examples of winter Antarctic sea-ice conditions are illustrated using SAR data from WWGS '92 Polarstern measurement locations. Figure 3 shows the 3 SAR frames chosen to compare the signatures of; rough, ridged and heavily deformed first-year ice (FYR) in a coastal regime; smooth, undeformed first-year ice (FYS) in the central Weddell Gyre; and mixtures of thick first-year and old second-year ice (FY/SY) in the north-western Weddell old-ice outflow region. Histograms in Fig. 4b highlight differences in signatures of relatively deformed and undeformed first-year ice. Peak in the FYS and FYR distributions differ by 3-4 dB, and it is apparent from the north-westernmost image that the winter FY/SY distribution is almost a convolution of the rough and smooth ice distributions. Though the winter backscatter signatures of SY and deformed FYR may be confused, Fig. 2 shows that their typical mean thicknesses are similar. Thus, from the simple perspective of discriminating thick and deformed ice from relatively thin, undeformed ice, winter SAR backscatter histograms appear to be a fairly useful indicator of the relative fractions of these component distributions and thus the areal distribution Weddell Sea ice thickness.

IV. TIME-SERIES OF FALL-FREEZE-UP

An advantage of EScat images is the capability to compile time-series of weekly average backscatter data. Figure 5 shows an example of ISW-1 data tracing values of *A* (solid line) and *B* (dotted line) between day 1 (1 Jan.) and day 88 (28 March), 1992. In each 7-day interval coefficients *A* and *B* are derived to describe a linear regression fit to data from all scatterometer imaging cells overlapping the fixed ISW-1 SAR-image location shown in Fig 1. The seven day window is then shifted and the fitting process repeated to describing σ^0 as a function of incidence angle θ and time. The lower panel of Fig. 5 illustrates changes in measured data as a function of time, with the single fitted *B* value from the upper panel used to estimate *A* for each scatterometer cell measurement. Resulting *A* estimates are shown as points in the lower, together with seven-day moving average shown as a thick line. Close correspondence of smoothed estimates of *A* with the fitted time-varying *A* values in the upper panel indicate success in reproducing trends observed in the original gridded backscatter data.

Figure 5 shows a period of EScat observations spanning the 3-day ice orbit phase. Fluctuations in summer surface conditions cause variations of several dB in *A* between days 1-8, and are similar in magnitude to changes described using SAR statistics in Fig 4a. Between day 8 and 21, there is a data blank which prevented the time-varying values of the two coefficients to be correctly estimated. After day 22, valid *A* and *B* values are calculated continuously until seven days before the end of the data on day 88. *A* values show a smooth increase and decrease of 2 dB between days 21 and 80, with a summer 40° backscatter maximum in the interval between days 44 and 47. The gradient *B* also rises and falls peaking at 0.22 dB/deg on day 32 (1 Feb.) then dropping in steps to a minimum of 0.135 dB/deg on day 64 (4 March).

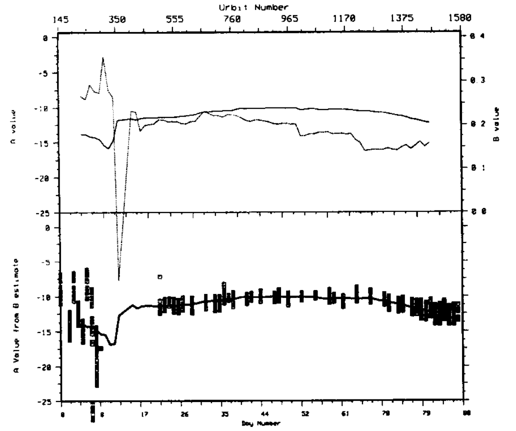

Figure 5. Fall freeze-up time-series of *A* and *B* coefficients, extracted from ERS-1 scatterometer images at a fixed location over the ISW drift track.

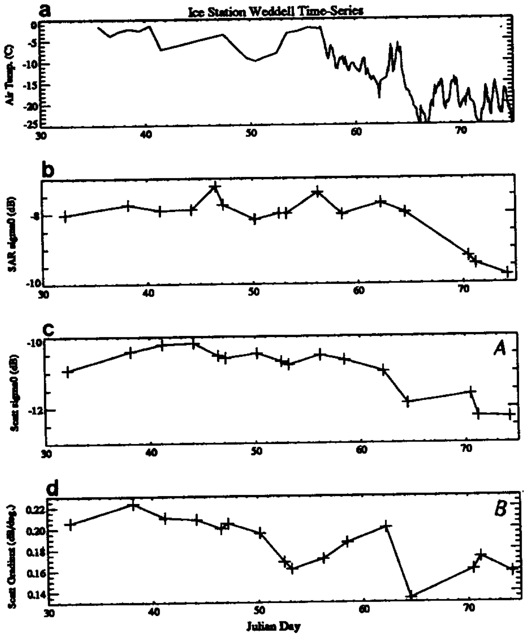

Figure 6. Comparison of ISW-1 temperature record with C-band SAR (20-26°) and Scatterometer backscatter time-series (40°) data.

To understand these seasonal changes, overlapping ISW-1 SAR image statistics are extracted and plotted in Fig. 6 with the ISW-1 air temperature record. Mean SAR image backscatter is plotted in Fig. 6b next to values of *A* and *B* (in Fig. 6c and d). Coregistered SAR backscatter values mimic the EScat seasonal trend almost identically with backscatter values consistently 3 dB higher than *A*.. The SAR similarly reaches a peak backscatter value on day 46, after which the variations are closely correlated with the ISW-1 air temperature records. Day 64 is particularly important, since it signals the onset of fall freeze-up, and Fig 6d shows a dramatic change in *B* indicating sensitivity to the changes induced by plummeting air temperatures.

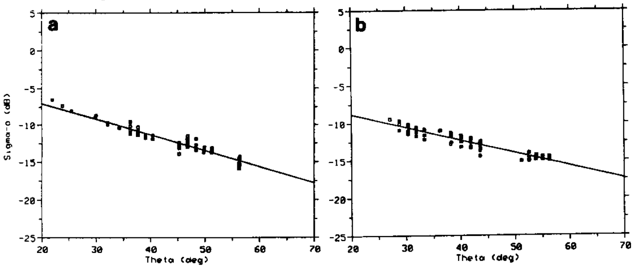

Figure 7. Weekly average ERS-1 scatterometer backscatter signatures derived on (a) day 32 (1 Feb.); and (b) day 70 (10 March).

Finally, Figures 7a and b illustrate the variation of backscatter with incidence angle, as derived from the EScat images from; (a) days 29-35; and (b) days 69-72. The regression line is used in each case to derive the values of *A* and *B* used in Figs. 5 and 6. Most importantly, these data clarify changes in the backscatter vs incidence angle relationship as seasonal changes take place. Fig. 7a has *A* and *B* values of -11.31 dB and 0.215 dB/deg, typical of the beginning of the time-series in Fig. 6. The contrasting plot in Fig. 7b indicates how near normal-incidence values decline, as the damp snow layer begins to freeze and the snow becomes more transparent to microwaves.

V. DISCUSSION

Results indicate that the EScat imaging technique complements and enhances lower frequency temporal and spatial ice coverage obtained by SAR. It does so by providing multiple incidence-angle C-band measurements, which can be used more effectively in discriminating ice-surface conditions. Future work will use shipborne WWGS '92 C-band scatterometer data to describe and illustrate local-scale radar scattering characteristics of the winter Weddell Sea pack ice. Together with ice property measurements made from the ship, these data can be exploited to evaluate the accuracy and utility of combining ERS-1 scatterometer and SAR images in estimating geophysical processes such as rates of new ice formation. EScat images clearly indicate the dynamics of the Weddell Gyre, and will be coupled with SAR images to monitor the mass flux of old ice out of the Weddell Sea during winter. Together these ERS-1 Active Microwave Instrument data can also be used to identify the main sources of ice production during the winter, and to clarify relationships between the advective and thermodynamic elements of Antarctic sea-ice advance and retreat.

VI. ACKNOWLEDGMENT

MRD performed this work at the Jet Propulsion Laboratory, California Institute of Technology under contract to the National Aeronautics and Space Administration; and DGL and DSE conducted their research at BYU. This research was made possible by funding from R. Thomas of NASA Polar Processes Program (Code YSC), and by ESA support of PIPOR proposal PIP.Ant3. ESA are gratefully acknowledged for ERS-1 SAR acquisition scheduling, and Jörg Gredel and the members of D-PAF for SAR product generation.

VII. REFERENCES

Drinkwater, M.R., D.G. Long, and D.S. Early, Enhanced Resolution Scatterometer Imaging of Southern Ocean Sea Ice, *ESA Journal*, 17, 307-322, 1993.

Long, D.G., D.S. Early, and M.R. Drinkwater, Enhanced Resolution Imaging of Southern Hemisphere Polar Ice. *Proc. IGARSS '94*, This Issue.

Drinkwater, M.R., and Ch. Kottmeier, Satellite Microwave Radar- and Buoy-Tracked Ice Motion in the Weddell Sea during WWGS '92. *Proc. IGARSS '94*, This Issue.